Japanese Journal of Applied Physics

The Japan Society of Applied Physics

PROGRESS REVIEW

Spintronics memory using magnetic tunnel junction for X nm-generation

To cite this article: Hiroshi Naganuma 2023 *Jpn. J. Appl. Phys.* **62** SG0811

View the article online for updates and enhancements.

You may also like

- First-principles studies of chromium line-ordered alloys in a molybdenum disulfide monolayer
N F Andriambelaza, R E Mapasha and N Chetty

- Control of anomalous Nernst effect in spintronic materials
Masaki Mizuguchi

- Order-Disorder Transition of Ternary Ordered Alloy
Zheng Maosheng, Liu Yunpeng, Gao Jiqiang et al.

This content was downloaded from IP address 130.34.56.1 on 22/05/2023 at 10:23

Japanese Journal of Applied Physics **62**, SG0811 (2023) **PROGRESS REVIEW**
https://doi.org/10.35848/1347-4065/accaed

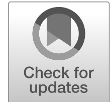

Spintronics memory using magnetic tunnel junction for X nm-generation

Hiroshi Naganuma[1,2,3*]

[1]Center for Innovative Integrated Electronics Systems (CIES), Tohoku University, Sendai, Miyagi, 980-8572, Japan
[2]Center for Science and Inovation in Spintronics (CSIS), Tohoku University, Sendai Miyagi, 980-8577, Japan
[3]Center for Spintronics Research Network (CSRN), Tohoku University, Sendai Miyagi, 980-8577, Japan

*E-mail: hiroshi.naganuma.c3@tohoku.ac.jp

Received December 12, 2022; revised April 3, 2023; accepted April 6, 2023; published online May 19, 2023

The feasibility of X nm-generation scaling with magnetic tunnel junctions (MTJs) in spintronic memory is aimed at keeping up with state-of-the-art transistor scaling. Magnetocrystalline anisotropy, shape magnetic anisotropy, and multi-interfacial magnetic anisotropy have been proposed to overcome thermal fluctuation even at the X nm-generation. The high magnetocrystalline anisotropy of the $L1_0$-ordered alloy combined with graphene as a tunneling barrier in the MTJs was the main concern in this study, and their potential for scaling for both 10 year data retention and nanosecond writing efficiency by micromagnetic simulation is investigated. Data retention of 10 years and high-speed writing of 2.2 ns are simultaneously achieved in the MTJs with a junction diameter of 7 nm. © 2023 The Japan Society of Applied Physics

1. Introduction

A von Neumann-type computer has a cache memory layer that works in conjunction with processor calculations to enable high-speed calculations. Data accumulated in the main memory from the high-speed memory layer is accumulated in the main memory before being non-volatilely accumulated in a large volume density memory such as a hard disk drive and/or NAND type flash memory. The cache memory layer, which directly interacts with the core processor, must be highly fast while simultaneously Requiring a large memory size and high-power consumption. In this way, the different types of memories have different roles in terms of speed and volume density. Among these, the cache and main memories are volatile, and the data disappears when the electric power is turned off. To maintain the data for interacting with the processor calculations, electric power is constantly supplied, thus increasing electrical consumption. Research on replacing these volatile memories with non-volatile memory is actively being carried out.[1–4] Magnetic random-access memory (MRAM), resistive RAM (ReRAM), and ferroelectric RAM (FeRAM) are major candidates for the next-generation of non-volatile memories. This study focuses on MRAM. The MRAM is one of the candidates considered to be promising in terms of both high-speed switching/reading and high-volume density.[2,5–7] So far, two types of MRAM have been intensively investigated, namely, spin–orbit-torque (SOT)-MRAM and spin-transfer-torque (STT)-MRAM, which differ in the writing method while the reading method by tunnel magnetoresistance (TMR) is the same. The SOT-MRAM is a 3-terminal memory and is characterized by high-speed writing of 0.35 ns by SOT.[8] The STT-MRAM is a two-terminal memory, which has the advantage of high volume density. Although each of the MRAMs has advantages, this study discusses the high-density STT-MRAM for targeting the X-nm generation. The STT-MRAM consists of magnetic tunnel junctions (MTJs), which are the non-volatile recording part. The MTJ has a three-basic-layer structure in which one ultra-thin insulating layer is sandwiched between two ferromagnetic layers. One of the ferromagnetic layers is a recording layer, and the other one is a reference layer. Currently, the insulating layer uses MgO, which provides a high TMR ratio owing to Δ_1-coherent tunneling.[9,10] Herein, as detailed in a later section, the MgO barrier is replaced by the graphene (Gr) barrier in order to introduce $L1_0$-ordered alloys as the recording layer. The typical operation mechanism for writing and reading in the MTJs is described as follows. The STT changes the magnetization direction (writing process) of the MTJs.[11,12] The charge current becomes a spin-polarized current by flowing through a ferromagnetic layer. When the spin-polarized current tunnels through the MgO barrier, spin polarization information is retained, and the magnetic recording layer receives the STT. The STT switches the magnetization direction of the recording layer. The role of STT changes depending on the direction of spin-polarized current flow, allowing the realization of the parallel (P)/antiparallel (AP) magnetization configuration of the recording layer. The STT is proportional to the current density; therefore, the charge current becomes small when the junction diameter of the MTJ becomes small, which is advantageous for reducing electric power consumption in scaling. For the reading process, the magnetization configuration of the P or AP states in the MTJs is read out through the TMR ratio.[13–16] The electrical resistance of the MTJs is low in the P state, and the electrical resistance of the MTJs is high in the AP state. The phenomenon in which the resistance changes depending on the P or AP states is the TMR effect. Although, depending on the circuit design and the application purpose, a TMR ratio of 100%–200% is generally required to reduce false readings. The reading sense current produced by the TMR effect is smaller than the switching current produced by the STT; therefore, a reduction of the switching current is required from the viewpoint of low electrical power consumption. With an embedded-MRAM using MTJs with junction diameters as small as 39 nm, electrical consumption was reduced by 97% compared with volatile memories.[17] An embedded-MRAM in which the MTJs are placed on the transistor can reduce electrical consumption and increase memory volume density. The electrical consumption in operation is only 47 μW for the two-transistor type of MRAM with a capacity of 64 kB using a 40 nm generation CMOS technology. This means that a microcomputer can operate with electric power generated by body temperature. The MRAM has potential advantages in edge computing owing to its low electrical consumption.[17–19] As mentioned above, the MTJs in the embedded-MRAM are placed directly on the transistor to shorten the distance, reduce

 © 2023 The Japan Society of Applied Physics

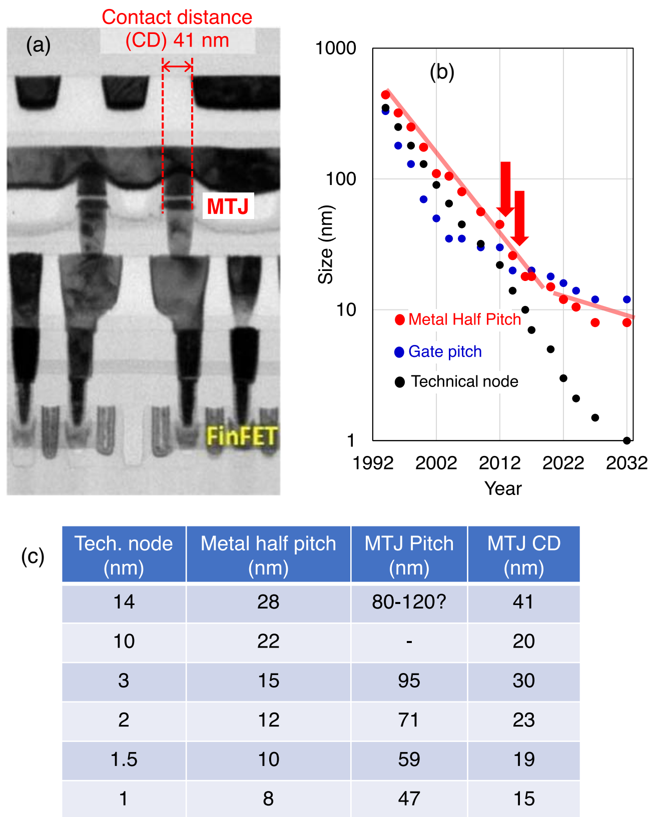

Tech. node (nm)	Metal half pitch (nm)	MTJ Pitch (nm)	MTJ CD (nm)
14	28	80-120?	41
10	22	-	20
3	15	95	30
2	12	71	23
1.5	10	59	19
1	8	47	15

Fig. 1. (a) MRAM with MTJ located directly on the FinFET transistor. The junction diameter of the MTJ was 41 nm. (b) Annual changes in metal half-pitch, gate pitch, and technical node in semiconductor microfabrication process. (c) The junction diameter of MTJ for scaling semiconductor microfabrication.

power consumption, and increase memory density.[20,21] In 2020, an IBM group demonstrated MTJs placed on a Fin FET (FinFET). [Fig. 1(a)].[20] In 2022, the Sk Hynix and Kioxia groups reported a further reduction in scaling, with a 45 nm pitch and a 20 nm junction diameter.[22] However, the junction diameter of the MTJs was still larger than that of state-of-the-art transistors. The scaling of MTJs should keep pace with the progress of state-of-the-art transistor microfabrication scaling. This means that further decreasing the diameter of the MTJ is required [Figs. 1(b) and 1(c)]. However, when the magnetic volume decreases to catch up with the scaling, the thermal fluctuation issue occurs in a ferromagnetic nature. To overcome the thermal fluctuation in the scaled MTJs, a large magnetic anisotropy is required. Nowadays, the interfacial perpendicular magnetic anisotropy (IPMA) CoFeB/MgO system is being used as a recording layer.[23] The CoFeB/MgO system is compatible with the Si wafer and the back end of the line (BEOL) process,[24,25] and thus, from the process point of view, the CoFeB/MgO system has industrial advantages. Figure 2 shows a schematic illustration of the scaling of MTJ to ensure data retention. At an MTJ junction diameter in 6X nm generation, a single CoFeB/MgO interface is enough to overcome thermal fluctuation. At an MTJ junction diameter below 40 nm, a single CoFeB/MgO interface is not enough to overcome thermal fluctuation. To overcome the thermal fluctuation below 40 nm, an increase in the number of interfaces by multi-layering CoFeB/MgO can result in an increase in the IPMA.[23,26,27] To increase the IPMA and suppress the thermal fluctuation, a double interface (Double-MTJs) was used in the 3X nm generation[28] and a quad interface (Quad-MTJs) was used in the 2X nm generation.[29] In the optimized stacking structure of the Quad-MTJs, even with a junction diameter of 18 nm, data retention of 10 years and rewriting times approaching 1 trillion were achieved simultaneously.[30] Moreover, the hexa-interface (Hexa-MTJs) demonstrated large thermal stability as well as solder reflow capability (260 °C) for targeting eFlash-type MRAM.[31] The multi-layering of the CoFeB/MgO interfaces is the de facto scaling standard technology. Another cutting-edge technology described in the red square in Fig. 2 is the shape magnetic anisotropy. By using a circular columnar recording layer elongated in the perpendicular direction, the shape magnetic anisotropy appears in the perpendicular direction.[32] This shape magnetic anisotropy increases as the MTJ junction diameter decreases in the same thickness, which has a strong advantage for scaling. For example, when the junction diameter is 7 nm, the thermal stability (Δ) can reach 40 at 12 nm thickness and 80 at 21 nm thickness. Then, the junction diameter of MTJs can be scaled to a few nanometers by employing the MTJs of a circular columnar recording layer with the shape magnetic anisotropy. Comparing the magnetic volume of the shape magnetic anisotropy to the multi-layered CoFeB/MgO interfacial magnetic anisotropy, the shape magnetic anisotropy needs a larger magnetic volume. With the increase of magnetic volume, the switching current by STT becomes large. As the circular columnar recording layer becomes longer, magnetization switching by the STT becomes complicated, so a proper aspect ratio is required for coherent magnetization switching.[33] Sufficient performance in terms of thermal stability in the X-nm generation is expected to be investigated for practical characteristics such as write endurance and write error rate (WER). At present, many of the reports that demonstrate data retention characteristics while simultaneously realizing high endurance and WER use the CoFeB/MgO multi-layered MTJs. A hybrid MTJ of the CoFeB/MgO IPMA and the shape magnetic anisotropy have also been proposed.[34] The hybrid MTJs may be one of the most promising structures because the total thickness and volume of the cylindrical recording layer can be reduced. The MgO tunnel barrier has the advantage of lowering electrical resistance due to Δ_1-coherent tunneling. However, tunneling electric resistance increases in the scaled MTJs. In particular, the electrical resistance tends to increase in the CoFeB/MgO multilayered-MTJs below 1X nm. This increases the load on the transistor, necessitating either increasing the diameter of the transistor or using two transistors to guarantee the current for STT switching below 1X nm. Thus, it is necessary to further reduce the electrical resistance of the MgO barrier. One method is to reduce the MgO thickness. The thickness of the MgO barrier has already been thinned down to 1 nm, which is 2–3 unit cells. This means that the MgO thickness reduction is close to the material limit. A two-dimensional (2D) material such as Gr is an example of a low-resistance tunnel barrier. The band structure of free-standing Gr has a Dirac cone that is gapless, which is not suitable for tunneling barriers. However, a gap appears in the Gr when the Gr comes into contact with the metals or the substrates.[35–38] Extensive research has been carried out on the formation of gaps and the types of van der Waals (vdW) forces at the metallic interface. This is because reducing the gap is necessary to use 2D materials in highly

© 2023 The Japan Society of Applied Physics

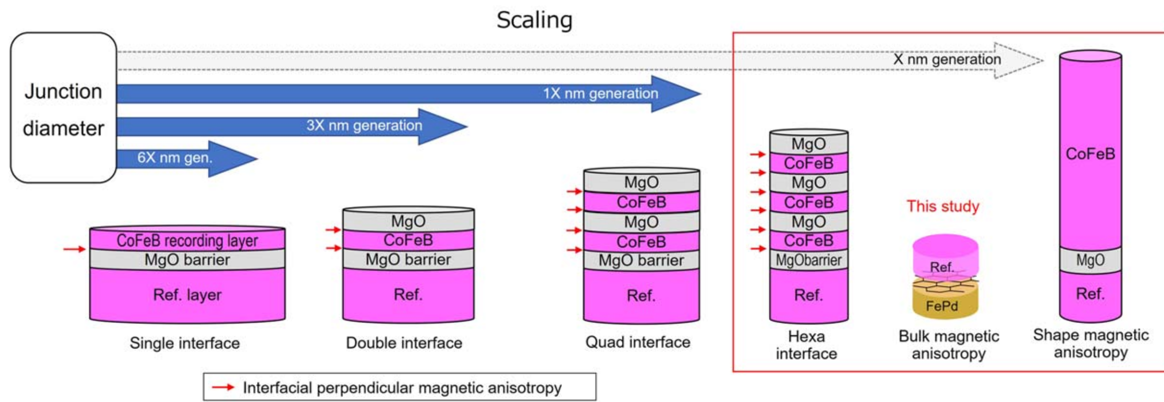

Fig. 2. The scaling of MTJ. As the MTJ diameter decreases by scaling, the number of CoFeB/MgO interfaces with interfacial magnetic anisotropy is increased to ensure data retention. The red square is the idea of X nm generation in scaling. In the X nm generation, the introduction of high bulk uniaxial magnetic anisotropy and shape magnetic anisotropy is being investigated in addition to CoFeB/MgO multi-layering of IPMA.

integrated transistors.[39] It has been predicted that Gr has the potential for low electrical resistance tunneling barriers in some ferromagnetic metal materials combinations. In the case of the TMR ratio of the Gr used as a tunneling barrier, a TMR ratio depends on the number of Gr layers. The TMR ratio increased with increasing the number of Gr layers until five Gr layers, and the maximum TMR ratio of approximately 900% is theoretically predicted by optimistic calculation.[40] Experimentally, in the early days of research on the MTJs with a Gr tunneling barrier, the TMR ratio was lower than the theoretical value.[41] From 2012 to 2021, the absolute value of the TMR ratio increased from a few percent[42–45] to tens of percent.[46,47] The magnetic electrodes of the MTJs were a combination of NiFe, Co, and Ni. The interface between these magnetic electrodes and the Gr barrier has a three-fold crystal symmetry, which is a highly compatible crystal symmetry. In 2022, a TMR ratio of 160% was experimentally reported at 2 K for Ni/Gr/Co-based MTJs.[48] If the upper Co electrode can be replaced by Ni, which is the same as the bottom electrode, theoretically, a 1000% TMR ratio is expected. The control of the crystal orientation for the upper electrode is more difficult than that for the lower electrode. This means, with additional technological development in the growth, the TMR ratio can increase to the theoretical value. Subsequently, an interface of different crystal symmetry bonded by the vdW force is described. Graphite is a layered material, and the chemical bond between layers is the vdW force. The vdW forces can be expected to cause Gr to be deposited on different crystal symmetries owing to its weak bonding nature. It might be possible to realize an MTJ stacking structure that ignores lattice misfit when using a Gr tunneling barrier.[49] As mentioned above, the CoFeB/MgO interface, the shape magnetic anisotropy, and their hybrid structure are candidates for the perpendicular magnetic anisotropy for scaled MTJs. As an alternative, the scaled MTJs using a combination of bulk $L1_0$-ordered alloys having a high magnetocrystalline anisotropy and vdW bonding of Gr are proposed.[50,51] Because the $L1_0$-ordered alloys have high magnetocrystalline anisotropy, and they can also simplify the stacking structure of the recording layer when compared with CoFeB/MgO multilayer system. $L1_0$-ordered alloys and MgO have around 10% lattice misfit, which degrades the interface flatness.[52] This large lattice misfit results in a reduction of the TMR ratio and the distribution of the magnetization direction at the interface. $L1_0$-ordered alloys cannot be used in combination with MgO tunnel barriers. To avoid this large lattice misfit, one of the ideas is utilizing the weak bond of the vdW force. Using an $L1_0$-ordered alloy as the recording layer and Gr as the tunnel barrier is a possible solution for obtaining low electrical resistance, a high TMR ratio, and strong thermal stability (data retention) in scaled MTJs. Furthermore, compared to CoFeB/MgO, shape anisotropic systems, and their hybrid structure, the volume of the recording layer is small in the $L1_0$-ordered alloys/Gr system, which is an advantage for a small STT-switching current. The structure and magnetic characteristics of the $L1_0$-ordered alloys/Gr crystallographic heterointerface have yet to be determined, and it is unclear if high-quality MTJs can be manufactured using the $L1_0$-ordered alloys/Gr system. Among the many $L1_0$-ordered alloys, $L1_0$-FePd has a small magnetic damping constant (α_{eff}) and is expected to reduce write power.[53]

In this study, the interfacial structure, and interfacial magnetic properties of the $L1_0$-FePd/Gr bilayer heterointerface were investigated and discussed with the aim of developing X-nm generation scaled MTJs. The data retention and writing characteristics of $L1_0$-FePd/Gr MTJs for the X nm generation were investigated using micromagnetic simulations. Two typical examples of MTJ junction diameters (10 nm and 7 nm) were investigated in detail by micromagnetic simulations.

2. Experimental methods

Figure 3(a) shows a schematic illustration of the sample preparation process.[49] Gr was formed by CVD, and $L1_0$-FePd films were grown on $SrTiO_3$ (001) substrates by rf magnetron sputtering. Once the samples were exposed to the atmosphere, they were transferred to the CVD chamber. The FePd films were heated to 600 °C in a 100 Pa H_2 atmosphere for 15 min to remove the surface oxidation layer. Surface oxidation was evaluated by X-ray photoelectron spectroscopy (XPS) and X-ray absorption spectroscopy (XAS) [Figs. 3(b) and 3(c)]. From the XPS measurement, it was confirmed that the oxidation peak of Fe disappeared after the hydrogen reduction treatment. Moreover, no Fe oxide peak was observed in the XAS spectrum using high-intensity synchrotron X-rays, indicating that the surface Fe oxidation layer was perfectly removed by the reduction process. The Gr growth by CVD method has an advantage compared with the

© 2023 The Japan Society of Applied Physics

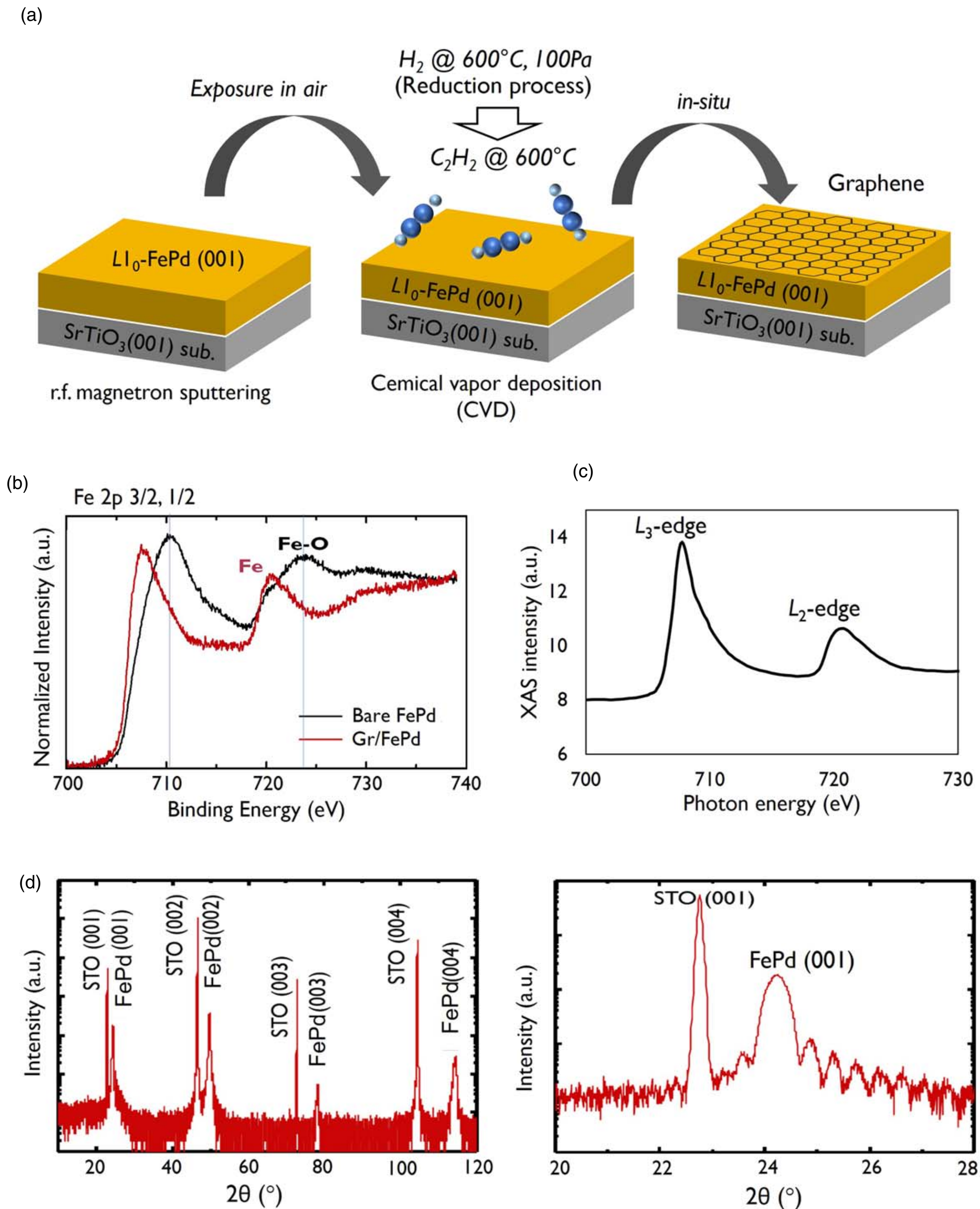

Fig. 3. (a) The deposition of the $L1_0$-FePd/Gr bilayer. The $L1_0$-FePd was grown on $SrTiO_3$ (001) substrate by rf magnetron sputtering, the sample was transferred to a CVD chamber, and graphene was formed after hydrogen reduction treatment in the CVD chamber. Reduction of the surface oxide layer on $L1_0$-FePd was confirmed by (b) X-ray photoemission spectroscopy (XPS) and (c) XAS. XAS was carried out in the synchrotron radiation (KEK, Photon Factory, BL-16). (d) The XRD profile of $L1_0$-FePd /Gr and its magnified pattern.

Gr transfer method because the reduction process and growth process can conduct in a vacuum chamber, which can prepare a high-quality interface. After H_2 was removed, the samples were exposed to a 1 Pa C_2H_2-atmosphere at 600 °C for 15 min, and then the Gr was formed on the FePd layer.

The structure was evaluated by X-ray diffraction (XRD; $\theta/2\theta$, Cu-Kα) and cross-sectional scanning transmission electron microscopy (STEM) observations. The X-ray magnetic circular dichroism (XMCD) of the Fe $L_{2,3}$-edges was measured to characterize the Fe states in the FePd layer. (@Photon factory; BL-16A).[54] Fluorescence X-rays emitted after XAS were acquired separately at different detection angles (θ_d) using a 1-megapixel soft X-ray CCD. The wavelength λ was estimated from the attenuation length (l) and the detection angle using the following relation: $\lambda = l \cdot \sin\theta_d$.[55] By analyzing a set of X-ray data recorded at different wavelengths, the depth-resolved XAS and XMCD spectra can be obtained. Magnetic anisotropy was analyzed by rotating θ_i. The θ_is of 90° and 30° mean that the magnetic field was applied at 90° and 30° from the in-plane direction, respectively. The applied magnetic field was 0.87 T.

A micromagnetic simulator (Examag, Fujitsu Ltd.) was used for calculations of the data retention and STT-switching characteristics. In the case of data retention, the

 © 2023 The Japan Society of Applied Physics

micromagnetic simulation incorporates the string method [56-60] combined with the climbing method. The hybrid of string and climbing methods is useful in identifying the minimum energy path between the P and AP states of the MTJs while decreasing the calculation costs. The energy barrier was divided into 40 images for data retention calculation. The magnetostatic energy (E_{sta}), anisotropy energy (E_{ani}), exchange energy (E_{exc}), and the sum of energy (E_{all}) are calculated at each point in the free energy landscape between bistable states. Note that the "energy curve" shown in this study is the result of searching for the minimum energy path for switching from the AP to P (P to AP) states. Herein, $\vec{a}_1$ and K_u are the unit vectors of the magnetic easy axis and the uniaxial magnetocrystalline anisotropy constant, respectively. Each energy can be described as follows.

$$E_{sta}(\vec{M}_F) = -\frac{1}{2}\vec{M}_F \cdot \vec{H} \tag{1}$$

$$E_{ani}(\vec{M}_F) = \frac{K_u}{M_{S,F}^2}(\vec{a}_1 \cdot \vec{M}_F)^2 \tag{2}$$

$$E_{exc}(\vec{M}_F) = \frac{A_s}{M_{S,F}^2}\{(\vec{\nabla}M_x)^2 + (\vec{\nabla}M_y)^2 + (\vec{\nabla}M_z)^2\} \tag{3}$$

$$E_{all} = \int dV\{E_{ani} + E_{exc} + E_d\} \tag{4}$$

$$K_i = K_u \cdot t_F + \frac{M_{S,F}^2 \cdot t_F}{2\mu_0} \tag{5}$$

where, $\vec{M}_F$, t_F, μ_0, and $M_{S,F}$ are the magnetization vector of the recording layer, the thickness of the recording layer, the vacuum permeability, and the saturation magnetization of the recording layer, respectively. It should be noted that the value of K_i described in this study does not include the demagnetizing field coefficient, $\left(\frac{M_{S,F}^2 \cdot t_F}{2\mu_0}\right)$.

For the STT-switching, it is necessary to take into account the STT associated with the spin-polarized current. Assuming tri-layer-based MTJs where the STT acts as the recording layer and the magnetic layer adjacent to the coupling layer is the reference layer, the LLG equation for the recording layer considering the STT acting between the multi-layer films is as follows.

$$\frac{\partial \vec{M}_F}{\partial t} = -\gamma[\vec{M}_F \times \vec{H}_{eff}] + \frac{\alpha}{M_{S,F}}\left[\vec{M}_F \times \frac{\partial \vec{M}_F}{\partial t}\right] + g(\theta)\frac{J_e\hbar}{2e}[\vec{M}_F \times (\vec{M}_R \times \vec{M}_F)] \tag{6}$$

$$g(\theta) = \frac{\rho_{0,R}}{t_F(M_{S,F} \cdot M_{S,R} + \lambda_F \vec{M}_F \cdot \vec{M}_R)}$$

where $\vec{M}_R$, γ, $\vec{H}_{eff}$, α, $M_{S,R}$, $g(\theta)$, J_e, $\hbar$, e, $\rho_{0,R}$ is the magnetization vector of the reference layer (T), the gyromagnetic ratio (m/A·S), the effective magnetic field, the damping constant, the saturation magnetization of the reference layer (T), the spin-transfer efficiency, the current density (A/cm^2), the Planck constant (J·S), the elementary charge (C), and the spin polarization, respectively.

The mesh size used in the stacking structure was set to 1.5 and 1.0 nm, considering the exchange bond length (l_{ex}).

$$l_{ex} = \sqrt{\frac{A_s}{H_k}} \tag{7}$$

where H_k is the magnetic anisotropy field. The mesh size of 1.5 or 1.0 nm is shorter than l_{ex}s in all calculation conditions. The IPMA was defined as a constant in the cylindrical area separated by boundaries with a thickness of 1 nm.

3. Results and discussion

3.1. $L1_0$-FePd/Graphene heterointerface

Figure 3(d) shows the $\theta/2\theta$ XRD patterns of a wide area and the enlarged area around the $SrTiO_3$ (001) peak for the $L1_0$-FePd/Gr on the $SrTiO_3$(100) substrate.[61] Only the diffraction peak of FePd (00 l) was observed, suggesting that the FePd film was epitaxially grown on the $SrTiO_3$ substrates and no other secondary phase was formed. FePd (00 l) was observed on the high-angle side of $SrTiO_3$ (00 l). It can be considered that the c-axis of FePd was shorter than the a-axis. This is because the FePd film was vertically compressed by $L1_0$-ordering. By compressing the c-axis, the $L1_0$-FePd exhibits the massive bulk PMA oriented in the c-axis. This means that controlling the orientation of the c-axis should be required in order to use the bulk PMA of $L1_0$-FePd as the recording layer. In this study, $SrTiO_3$ (100) substrates were used to elucidate the potential of the $L1_0$-FePd, but there have also been studies on growing $L1_0$-ordered alloys on SiO_2/Si (100) substrates[62,63] and on the TiN electrode.[64–67] These reports indicated that the c-axis orientation of the $L1_0$-ordered alloy can be controlled with high quality by selecting the appropriate buffer layer and optimizing the growth conditions. Therefore, buffer layers are used instead of the $SrTiO_3$ substrate when the $L1_0$-FePd is integrated into the three-dimensional (3D) structure of the transistors. The preparation window integrated into the 3D structure of $L1_0$-FePd might be severe compared with the CoFeB/MgO system. Expanding the XRD diffraction peak around the (001) of FePd, the satellite reflection peaks were clearly observed around the main (001) peak, indicating that the interface between the $L1_0$-FePd and the Gr was flat.

To directly analyze the interfacial atomic structure of the $L1_0$-FePd/Gr crystallographic heterogeneous interface, cross-sectional STEM observation was carried out. Two STEM detectors, annular bright-field (ABF), and high-angle annular dark-field (HAADF), were used to analyze light and heavy elements simultaneously. As shown in Fig. 4(a), the ABF detector placed inside has an advantage for detecting light elements, such as carbon, which have small diffraction angles. On the other hand, HAADF has an advantage for detecting heavy elements, such as Fe and Pd, which have large diffraction angles. The two detectors are required for the structural analysis of $L1_0$-FePd/Gr, which consists of light and heavy elements. Figure 4(b) shows the cross-sectional ABF and HAADF-STEM images at the heterointerface of the $L1_0$-FePd/Gr bilayer. An overlapping contrast of black dots was observed at the locations of the three orange arrows in the ABF-STEM image. The contrast disappeared in the HAADF-STEM image, indicating that the Gr layer is located

 © 2023 The Japan Society of Applied Physics

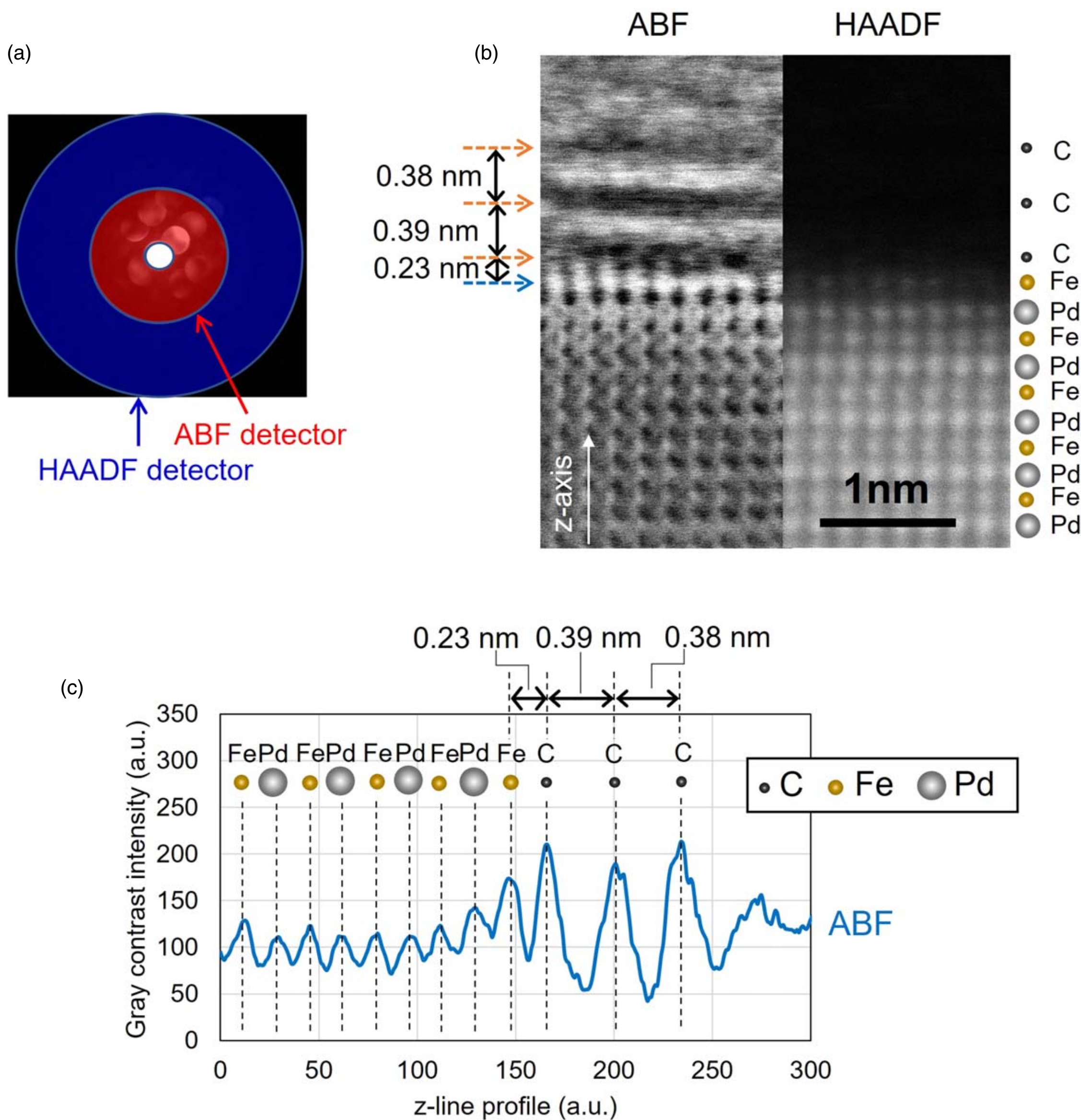

Fig. 4. (a) ABF and HAADF detector using STEM observation, (b) cross-sectional STEM image of ABF and HAADF detector; (c) line profile of the *z*-axis using the ABF-STEM image. The three Gr layers were confirmed, and the interlayer distance between Fe and C was 0.23 nm.

at the position of the orange arrows. Figure 4(c) shows the line profile evaluated from the ABF-STEM image. The origin of the z-profile was the lower edge of the ABF-STEM image in Fig. 4(b). The gray contrast of Fe and Pd was observed from the ABF-STEM line profile, which is consistent with the alternatively arranged Fe and Pd atoms clearly observed in the HAADF-STEM image. The alternate arrangement of Fe and Pd atoms on the *z*-axis (perpendicular direction) means that the $L1_0$-ordering is high. The STEM observation area had a three-layer Gr. The interlayer distances of this three-layer Gr were 0.38 and 0.39 nm, which are close to the interlayer distances of bulk graphite. The interlayer distance between $L1_0$-FePd and Gr was as short as 0.23 nm.

The shortening of the interlayer distance (0.23 nm) between Gr and $L1_0$-FePd was elucidated using a first-principles calculation. According to the calculations of the interlayer distance between the Gr and Ni and the Gr and Co with three-fold symmetry, which is compatible with the crystal symmetry, [Fig. 5(a)][47] the interlayer distance of the Gr varies depending on the contacting metal materials as well as the atomic positions. Regarding Co, the interlayer distance becomes longer when Co is rotated. The calculation example of the interaction energy of *h*-BN and Co indicates that there are two kinds of vdW forces between Co and *h*-BN: chemisorption and physisorption types [Fig. 5(b)].[68,69] These two vdW forces are correlated with the interlayer distance, and the minimum value of the interaction energy moves from physisorption to chemisorption as the distance decreases. This fact is considered to be qualitatively common to 2D materials bonding in the vertical direction by vdW forces. It is suggested that the vdW bonding changes depending on the metal and the relative positional relationship of the atoms. However, the interfacial structure between Gr and $L1_0$-FePd at the crystallographic heterointerface is more complicated than that of the Co and Ni cases. The interfacial atomic positions of the heterointerface were predicted by first-principles calculations for the $L1_0$-FePd/Gr.[70] First-principles structural optimization using the VASP code with PBE39 was performed for exchange correlation, and Grimme's DFT-D2 method40 was used for

 © 2023 The Japan Society of Applied Physics

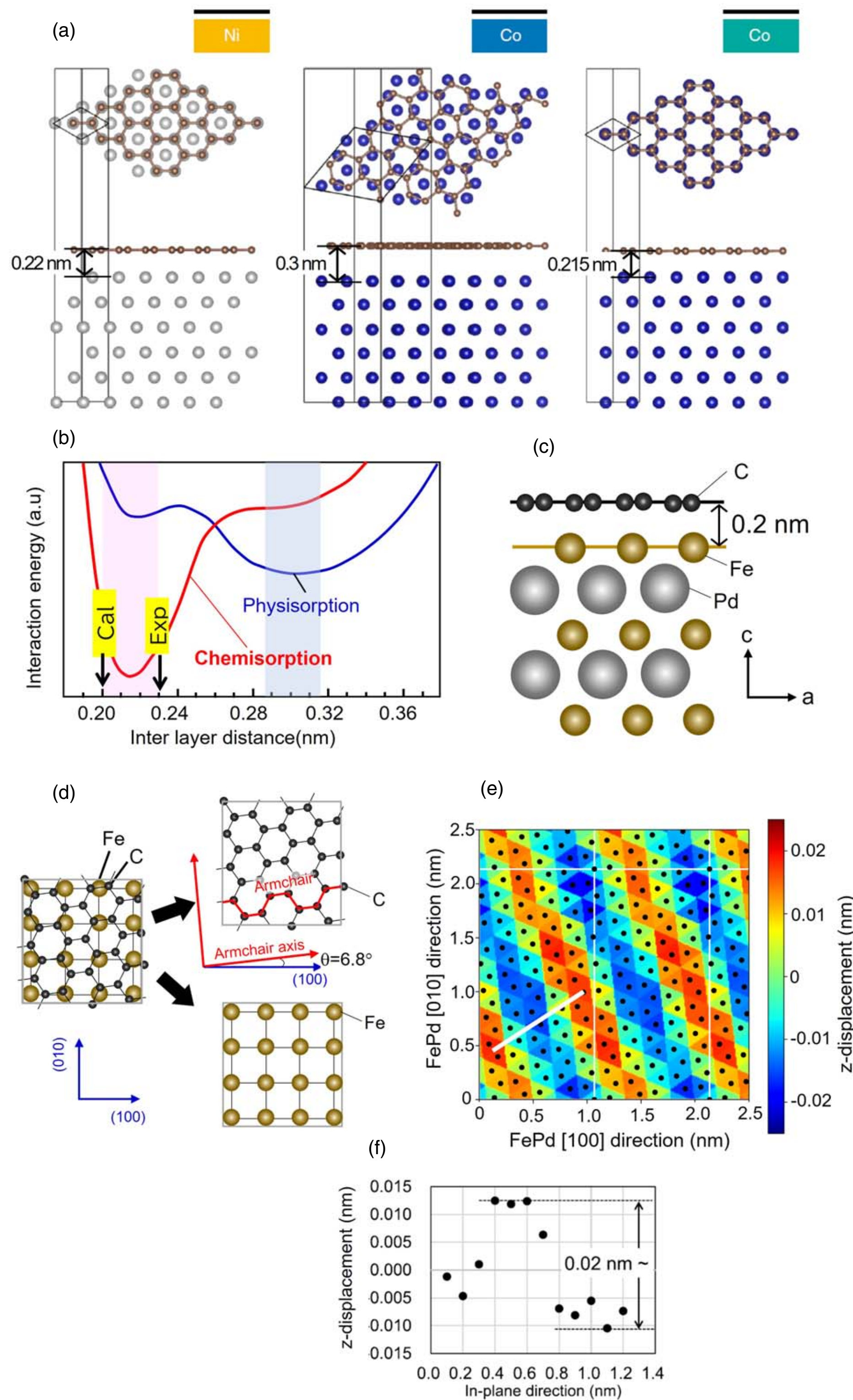

Fig. 5. (a) Ab-initio calculated layer separation for the three configurations bonded by vdW force: epitaxial Ni/Gr interface rotated and epitaxial Co/Gr interface. The rotated Co/Gr interface exhibits a weak interaction similar to that expected for the low-temperature evaporation of a top Co electrode on graphene. (b) Interlayer distance based on layer-to-layer interaction energy for two types of vdW forces. The physisorption-type vdW is a weak bonding, and the chemisorption-type vdW force is considered to be a relatively strong interlayer bond with orbital hybridization. The interlayer distance between 2D materials and metals is determined by the relative positions of atoms and the kinds of material. The schematic illustration of the interfacial structure of $L1_0$-FePd/Gr, which is a different crystal interface, was optimized by first-principles calculation. The interlayer distance is 0.2 nm of Chemisorption-type vdW forces. (d) The top-view of the $L1_0$-FePd/Gr heterointerface. The first layer of Gr and the Fe layer of $L1_0$-FePd are shown, and the separated two layers are indicated. Gr's armchair axis is rotated 6.8° concerning $L1_0$'s 100. (e) z-direction displacement mapping of the first layer of Gr.

the vdW interaction. The interlayer distance between Fe atoms on the outermost surface of $L1_0$-FePd and Gr was found to be 0.2 nm [Fig. 5(c)]. Therefore, the Gr and the $L1_0$-FeFd are considered to be chemisorption-type vdW forces, which have strong orbital hybridization. Next, the atomic positions at the interface between Gr and $L1_0$-FePd are calculated. The Gr armchair axis was found to have the lowest interfacial energy when $L1_0$-FePd is rotated by 6° in

© 2023 The Japan Society of Applied Physics

the in-plane direction [Fig. 5(d)]. To understand the adsorption force, the energy change on moving Gr in the x and y-axis directions was calculated. The maximum value of the energy change was only 0.006 eV atom^{-1}, which is one order of magnitude smaller than 0.04 eV atom^{-1} for the Gr/Ni (111) system. This small energy change implies that the adsorption of $L1_0$-FePd/Gr has physical adsorption. In addition, it was found that the strain in the Gr honeycomb structure was considerably smaller for the in-plane direction by calculating the 20 conditions under which supercells are automatically generated.

The carbon in the Gr is slightly displaced in the z-direction in the case of the perpendicular direction. As shown in Fig. 5(e), the z-direction displacement of carbon is periodic. The z-displacement of the white bar with the largest z-displacement in Fig. 5(e) is shown in Fig. 5(f). The periodic z-displacement is thought to be caused by the vdW force of chemisorption-type with the dispersion of bond angles and bond lengths at the crystallographic heterogeneous interface. The amplitude of the z-displacement is the sub-angstrom range, and the periodicity appears to be moiré interference fringes.

A notable point of the first-principles calculations for scaled MTJs is that a strong orbital hybridization owing to the chemisorption-type of the vdW force is predicted. The chemisorption-type is induced by the shortening of the interlayer distance, which is due to the overlapping of the orbitals in the perpendicular direction, causing the bonds to become stronger. This anisotropic orbital overlapping in the perpendicular direction suggests the induction of IPMA. The IPMA was reported in Gr with a Co or Ni bilayer.[71–75] Next, depth-resolved XMCD was used to evaluate the interfacial magnetic property of the $L1_0$-FePd/Gr. The surface-sensitive magnetic information could be obtained using a soft X-ray. Figure 6(a) shows the depth-resolved XMCD spectrum around the Fe $L_{3,2}$-edges for the $L1_0$-FePd/Gr. The magnetic field was applied in the perpendicular direction ($\theta_i = 90°$). The depth information was from 0.25 to 2.5 nm. The spin (M_s) and orbital (M_l) magnetic moments were analyzed using the sum rule. The values obtained from the XMCD of the interface and inner layer indicated that M_s at the interface decreased and M_l increased for $\theta_i = 90°$. To investigate the presence or absence of magnetic anisotropy, the external magnetic field was tilted. Figure 6(b) shows the depth-resolved XMCD spectrum for the tilted direction ($\theta_i = 30°$). Because the amount of M_s on the interface differs from that on the inner layer, the magnetic anisotropy was analyzed using their ratio (M_s/M_l) at $\theta = 90°$ and 30°. Focusing on M_s/M_l at the interface, a strong magnetic anisotropy was observed at 90°, which is the perpendicular direction. This means that the IPMA was induced at the $L1_0$-FePd/Gr heterointerface. The important result is that $L1_0$-FePd itself possesses a high bulk magnetocrystalline anisotropy, and the IPMA direction is the same as that of the bulk magnetocrystalline anisotropy direction, so the two magnetic anisotropies have an additive relationship. Thus, the summation of bulk PMA and IPMA effectively overcomes thermal fluctuation when the MTJ is miniaturized.

3.2. Micromagnetic simulation for X-nm generation

The micromagnetic simulation was performed to determine how much MTJs can be scaled while maintaining data retention capabilities for 10 years utilizing the $L1_0$-FePd/Gr system. Analysis of the depth-resolved XMCD fitting showed that the thickness of IPMA was 1 nm.[61] The thickness of IPMA is nearly consistent with the Gr/Co system. The IPMA of $L1_0$-FePd/Gr had changed abruptly rather than gradually. The IPMA was set to uniform with a thickness of 1 nm from the interface for the micromagnetic simulation [Fig. 7(a)]. The magnetocrystalline anisotropy constant (K_u) of $L1_0$-FePd is 2 MJ m^{-3},[76,77] the saturation magnetization (M_s) is 1.2 T, and the exchange stiffness constant (A_s) is 6 pJ m^{-1}.[76] The K_u, M_s, and A_s at around 300 K were estimated from the magnetization curves at RT and the fitting of the temperature dependence of M_s and A_s for the $L1_0$-FePd epitaxial film. The IPMA constant of $L1_0$-FePd/Gr is set to be 1 MJ m^{-2}, which is the same as that of the IPMA of Gr/Co.[71] The IPMA of 1 MJ m^{-2} is almost the same as the IPMA constant of the CoFeB/MgO system.[23] This suggests that 2D materials can be expected to have a high IPMA, similar to the CoFeB/MgO system. Several studies on IPMA for 2D materials have been reported,[71–75] and IPMA appears not only in Gr but also in h-BN, etc. The weak bonding of vdW forces in the 2D materials allows these materials to be free from the constraint of lattice misfit caused by crystallographic heterointerface, which allows a great opportunity to use advanced materials for the recording layer. Here, the calculation of Δ using micromagnetic simulations is described to better understand the performance of scaling. Figure 7(b) shows the magnetization curve calculated by micromagnetic simulation. A magnetic field was applied in the perpendicular direction. To reduce the computational cost of determining the Δ, only the neighborhood where magnetization switching occurs is extracted. For example, the magnetization curve has 913 data points, and the magnetization switching from the AP to P state is approximately half of that, at 455 points. The magnetization curve has a sharp magnetization switching, and the magnetization switching from AP to P is realized only at 9 data points. The computational cost can be reduced by using 9 sharply switched magnetization data points for the barrier height calculation rather than all the data points from AP to P. There are two types of energy barrier calculations: switching from P to AP states and from AP to P states. In this calculation, as indicated by the arrow in Fig. 7(b), the calculation of Δ is mainly carried out by switching from the AP to the P states. Figure 7(c) depicts an energy curve from the AP to the P state. The vertical axis is energy (J), and the index of data retention Δ is calculated by a simple equation as follows:

$$\Delta = \frac{(E_{max} - E_{min})}{K_B T} \tag{8}$$

Δ is an index of thermal stability, and when Δ of 54 is needed, it indicates 10 years of data retention time for a 0.1 ppm failure rate of 1 Mbit memory.[78] In other words, a Δ of 54 enables 1 Mbit of memory to be no error. To investigate the thermal stability of the X-nm generation of MTJs, the junction diameter of MTJs was systematically investigated between 3 nm and 70 nm. The $L1_0$-FePd film thickness varied from 0.4 nm, which is almost the same size as one unit cell of $L1_0$-FePd, to a maximum of 7 nm. Therefore, the contribution of shape magnetic anisotropy is almost negligible. To understand the effect of IPMA induced

© 2023 The Japan Society of Applied Physics

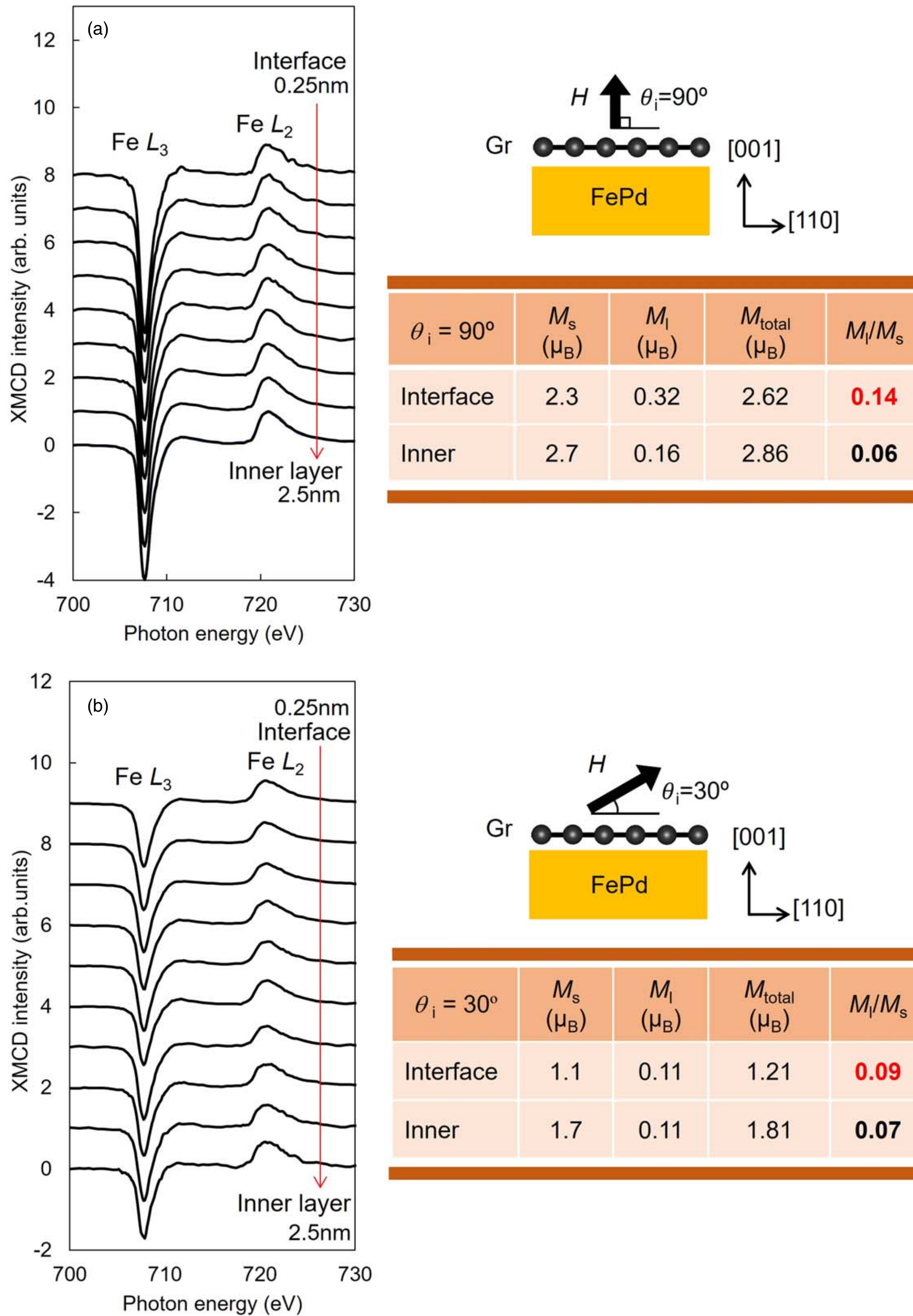

Fig. 6. Depth-resolved XMCD spectra for a magnetic field applied to (a) perpendicular direction ($\theta_i = 90°$) and (b) tilted direction ($\theta_i = 30°$). The spin (M_s) and orbital (M_l) magnetic moments and their summation (M_{total}) and ratio (M_l/M_s) are calculated by the sum rule.

by Gr, Δ was calculated with and without Gr on the $L1_0$-FePd. Figure 8(a) shows the $L1_0$-FePd film thickness dependence of Δ for various junction diameters in the case of $L1_0$-FePd/Gr. Δ tends to decrease monotonically as the $L1_0$-FePd film thickness decreases at all junction diameters. In the case of a junction diameter of 3 nm, it seems difficult to achieve 10 year data retention by increasing the film thickness, even if the effect of shape magnetic anisotropy with an aspect ratio of around 2.2 is taken into account. A large shape anisotropy is required by further increasing the aspect ratio to achieve Δ of 54 for a junction diameter of 3 nm. From these facts, it can be considered that the magnetic anisotropy consisting of only bulk PMA and IPMA in the $L1_0$-FePd/Gr bilayer is not very effective for a junction diameter of 3 nm. The shape of magnetic anisotropy requires a junction diameter smaller than 3 nm. The data retention

© 2023 The Japan Society of Applied Physics

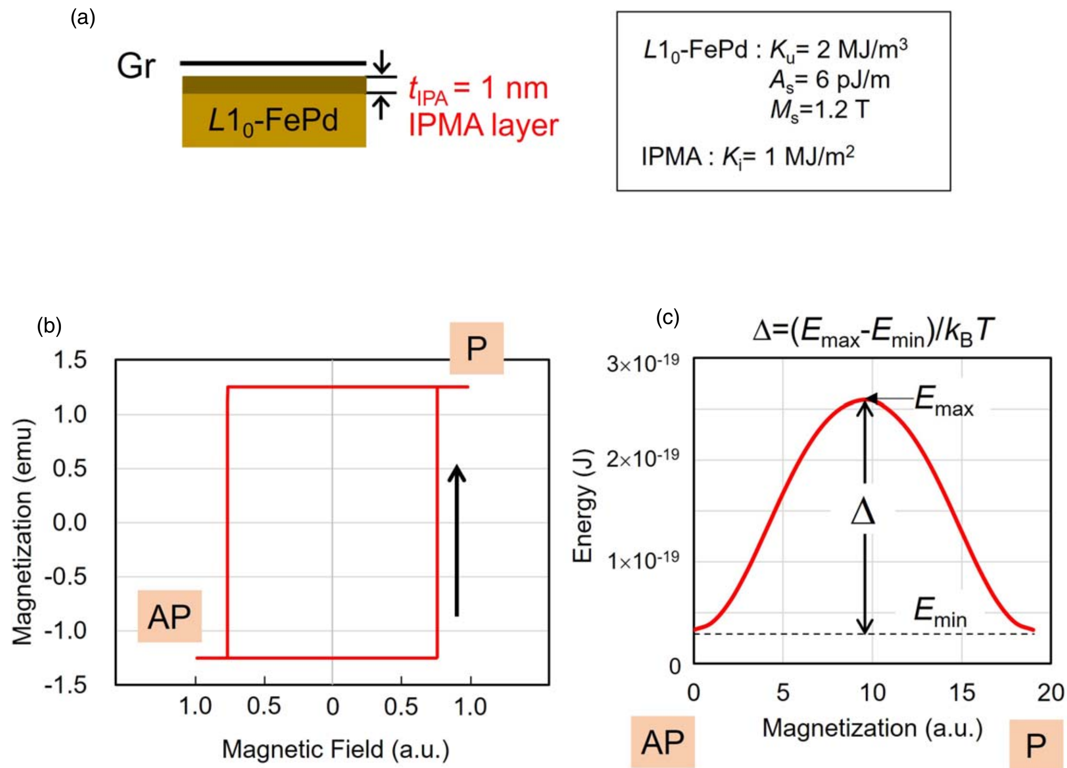

Fig. 7. (a) Schematic illustration of the cross-sectional image and magnetic parameters of $L1_0$-FePd/Gr used for micromagnetic simulation; (b) simulated magnetization curve; and (c) simulated energy barrier switching from AP to P state. The energy barrier in (c) is calculated using the switching region indicated by the arrow in the magnetization curve in (b). Δ is calculated by subtracting E_{min} from E_{max} and then dividing by $k_B T$. T is 300 K.

above 10 years with a Δ of 54 is guaranteed at a junction diameter of 7 nm and a thickness of 3 nm. If the junction diameter is further increased to 10 nm and 30 nm, Δ becomes even larger. Based on the data in Fig. 8(a), the relationship between the junction diameter and Δ was rearranged in Fig. 8(b). The magnification of Fig. 8(b) was shown in Fig. 8(c). From Fig. 8(c), the Δ does not reach 54 for the film thickness of 0.4 nm even if the junction diameter is increased to 30 nm. The $L1_0$-FePd film thickness of 0.4 nm is the size of a unit cell, and it is expected that it will be difficult to grow a uniform film of this thickness over a wide area using the sputtering deposition method. To achieve Δ of 54 for a film thickness of 1 nm, the junction diameter must be an unrealistic value. Δ becomes 54 with a junction diameter of 10 nm and a film thickness of 2 nm, which is the realistic aspect ratio for the thickness/junction diameter of the MTJs from the viewpoint of the fabrication process. Figure 8(d) shows the relationship between the junction diameter and the $L1_0$-FePd film thickness for Δ in MTJs without Gr. The $L1_0$-FePd MTJ without Gr has no IPMA but bulk magnetocrystalline anisotropy. The difference of Δ between $L1_0$-FePd/Gr and $L1_0$-FePd is approximately 7%–10%. In this research, the target of scaling is the X-nm generation of MTJs in order to examine the possibility of being able to follow the fabrication process of the most advanced scaled transistors. Therefore, a junction diameter of 7 nm with a thickness of 3 nm was selected for further detailed investigation. For comparison, MTJs with junction diameters of 10 nm (thickness of 2 nm) were also investigated.

Figure 9 shows the E_{all} profiles between the AP and P states separated into E_{sta}, E_{ani}, and E_{exc}. E_{all} is the summation of E_{sta}, E_{ani}, and E_{exc}. Figure 9(a) shows the energy barrier without the Gr on the $L1_0$-FePd at a junction diameter of 10 nm and a film thickness of 2 nm. During the process of magnetization switching from the AP to the P state, the magnetization is once oriented in the in-plane direction, which results in an increase in the demagnetizing field and a decrease in the magnetic anisotropy. The exchange coupling energy is maximized in the middle of the switching process of magnetization because of domain wall formation during the switching. The asymmetry of the energy barrier curves is due to the stray magnetic field from the reference layer. This asymmetry could disappear by suppressing the stray magnetic field from the reference layer. Figure 9(b) shows the energy barrier for the Gr on the $L1_0$-FePd. The IPMA, with a thickness of 1 nm, is formed at the interface on the $L1_0$-FePd side. Δ increased from 47 to 52 due to the addition of IPMA at the Gr on the $L1_0$-FePd interface. The shape of the energy barrier was the same as that without the Gr case. Figures 9(c) and 9(d) show the energy barrier curves for a junction diameter of 7 nm and a film thickness of 3 nm on the $L1_0$-FePd with Gr and without Gr, respectively. The mesh size should be shorter than the exchange coupling length, as mentioned in the experimental procedure. A mesh size of 1.5 nm is smaller than the exchange coupling length as described in Eq. (7). To ensure this mesh size has no influence, calculations were carried out for both mesh sizes of 1.5 nm and 1.0 nm in the case of a junction diameter of 7 nm and a film thickness of 3 nm. The results show almost no change between 1.0 and 1.5 nm. Δ increased from 53 to 57 in the case of Gr, and 10 year data retention is obtained in a realistic MTJ structure with a junction diameter of 7 nm and a film thickness of 3 nm. The IPMA layer at the interface and the inner layer are magnetically coupled, and the

 © 2023 The Japan Society of Applied Physics

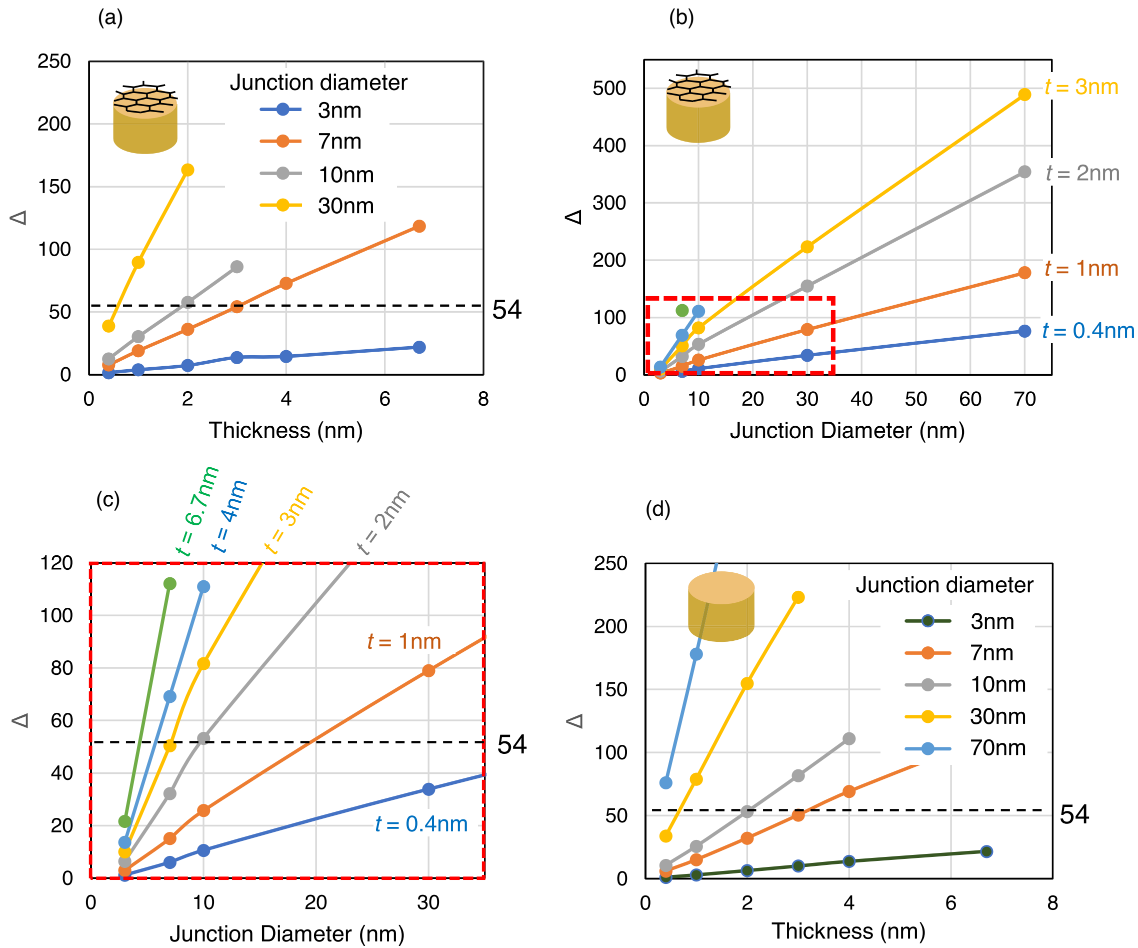

Fig. 8. Micromagnetic simulation of (a) $L1_0$-FePd thickness dependence of Δ with various junction diameters, (b), (c) $L1_0$-FePd junction diameter dependence of Δ with various film thicknesses for the $L1_0$-FePd/Gr, and (d) $L1_0$-FePd film thickness dependence of Δ with various junction diameters for the $L1_0$-FePd.

magnetization is switched almost simultaneously. This suggests that $L1_0$-FePd/Gr can be expected to meet the needs of the recording layer and tunnel barrier layer for the X-nm generation from the viewpoint of data retention characteristics.

Data retention for more than 10 year can be achieved at the 7 nm junction diameter, which is within the targeted range of the X-nm generation. Next, the high-speed STT magnetization switching characteristics were investigated. Figure 10 shows the STT magnetization switching properties of $L1_0$-FePd/Gr/[Co/Ir]x MTJs at various applied voltages. The [Co/Ir]x is a multi-layer that is used as the perpendicularly magnetized synthetic reference layer.[79,80] This synthetic magnetic structure can effectively suppress the stray magnetic field, which reduces asymmetric STT-switching. A 5 ns square wave pulse was applied to examine the high-speed STT switching characteristics. A waiting time of 5 ns was set before applying the pulse to stabilize the magnetization of $L1_0$-FePd and Co by interlayer magnetic interaction. $L1_0$-FePd is assumed to be a metallic conductor. It was reported that the resistance-area (RA) product of the Gr tunnel barrier can be lowered to 1.5 $\Omega{\cdot}\mu\text{m}^2$ by suppressing the oxidation that forms at the Gr interface with the metal layer.[81] As shown in Fig. 4(b), no oxidation was observed at the $L1_0$-FePd/Gr interface, so the $L1_0$-FePd/Gr interface can also be considered to have a low RA such as 1.5 $\Omega{\cdot}\mu\text{m}^2$. Note that, depending on the number of layers of Gr, a further reduction of RA is expected. The spin polarization of $L1_0$-FePd was set to 0.56 on the assumption of the Fe termination. Other magnetic parameters were the same as those used in the calculation of Δ. The applied voltage to the MTJs was changed between 0.4 and 3.0 V, and data points were not plotted if no switching occurred within 5 ns. The magnetization values on the vertical axis include all of the recording layer and the reference layer and are the values after subtraction. Figure 10(a) shows the STT-switching curves for the recording layer of the $L1_0$-FePd and the $L1_0$-FePd/Gr in the MTJ, which have a junction diameter of 10 nm. In Fig. 10(a), the magnetization changed from the AP state to the P state. In all cases, the STT-switching is steep, which suggests the high efficiency of STT-switching was performed in both $L1_0$-FePd and $L1_0$-FePd/Gr. As the voltage decreased, the time required for switching became longer. The following equation expresses the switching voltage (V_c):

$$V_c = \frac{2e\alpha}{\hbar P} RA \mu_0 M_s t_{rec} H_k^{eff}, \tag{9}$$

where α, $\hbar$, P, RA, μ_0, M_s, t_{rec}, and H_k^{eff} are the damping constant, Dirac's constant, spin polarization, RA productions, permeability in vacuum, saturation magnetization, recording layer thickness, and effective anisotropy field, respectively.

The following equation expresses the switching speed (t_{switch}) in the perpendicularly magnetized MTJs:

© 2023 The Japan Society of Applied Physics

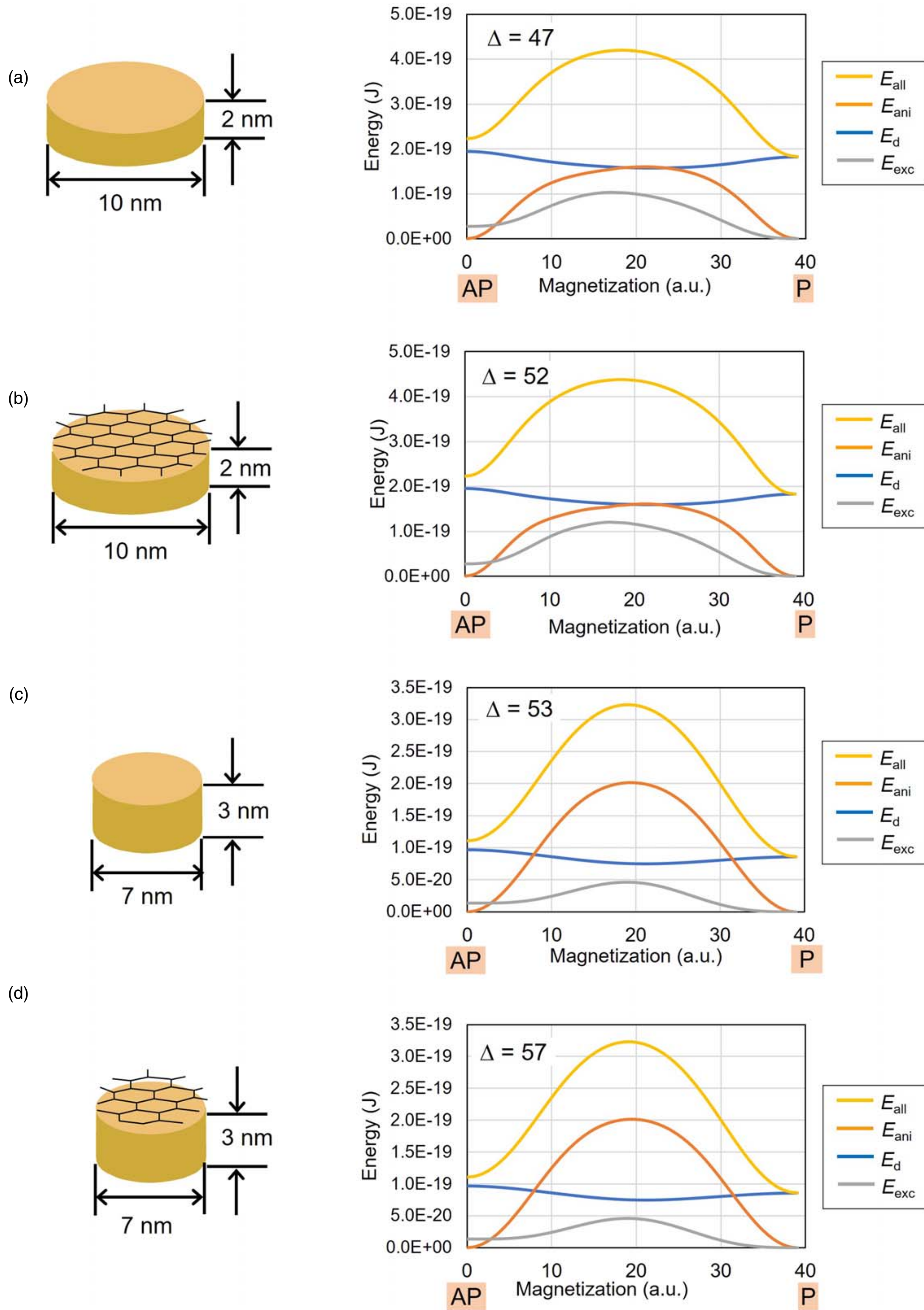

Fig. 9. Micromagnetic simulation of the total energy (E_{all}) is divided into anisotropic (E_{ani}), magnetostatic (E_{st}), and exchange coupling (E_{ex}) energies for (a) $L1_0$-FePd, and (b) $L1_0$-FePd/Gr with a junction diameter of 10 nm and a thickness of 2 nm. (c) E_{all} is divided into E_{ani}, E_{st}, and E_{ex}, and for (c) $L1_0$-FePd, and (d) $L1_0$-FePd/Gr with a junction diameter of 7 nm and a thickness of 3 nm.

$$t_{switch} \approx \tau \frac{1}{V-1} \mathrm{In}\left[\frac{2\Delta E}{k_B T}\right], \tau = \frac{1+\alpha^2}{\alpha\gamma\mu_0 H_k^{eff}} \mathrm{In}\left[\frac{2\Delta E}{k_B T}\right], \quad (10)$$

where τ, V, Δ, γ are the relaxation time, applied voltage, thermal stability factor, and gyromagnetic ratio, respectively. Figure 10(b) shows the switching start time at each applied voltage adjusted to the 3.0 V start time. The magnetization was slowly switched as the voltage decreased. This is because the voltage is in the denominator of Eq. (10). On the other hand, the incubation time, which is the time until switching starts after the pulse application, also depends on the applied voltage. The incubation time increased with decreasing applied voltage. Figure 10(c) shows the relationship between the STT-switching time and the applied voltage estimated from the switching curves for both AP to P and P to

© 2023 The Japan Society of Applied Physics

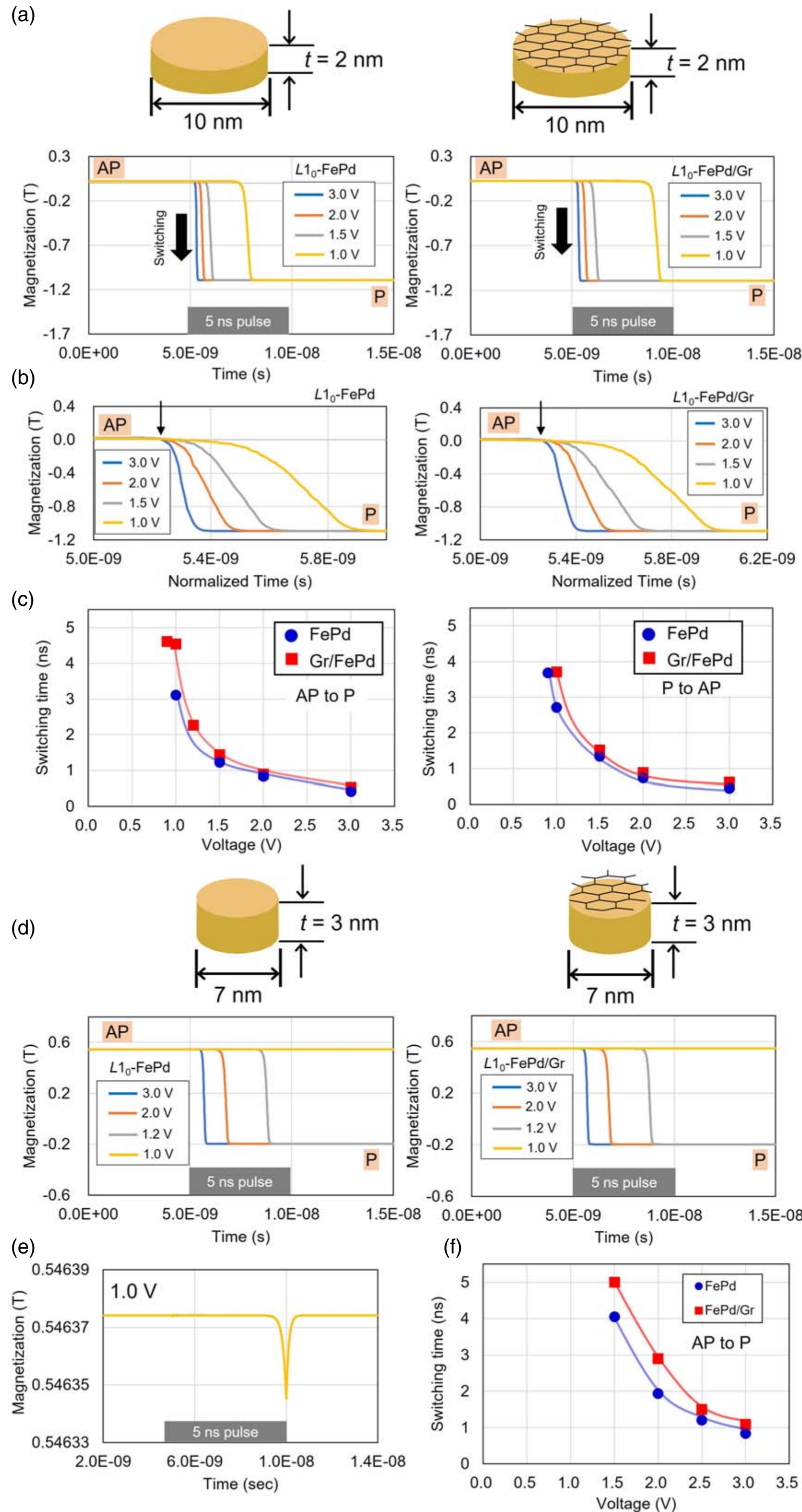

Fig. 10. Micromagnetic simulation of (a) STT switching behavior of $L1_0$-FePd and (b) $L1_0$-FePd/Gr with various applied voltages, (b) STT switching behavior normalized by the start time of STT switching at 3 V, (c) applied voltage dependence of switching time calculated from STT switching curves in (a) for the junction diameter of 10 nm and thickness of 2 nm. The STT switching behavior of (d) $L1_0$-FePd and (e) $L1_0$-FePd/Gr with various applied voltages for the junction diameter of 7 nm and thickness of 3 nm. (e) The STT switching behavior when STT switching is not completed with an applied voltage of 1.0 V. (c) Applied voltage dependence of switching time calculated from STT switching curves in (d). The STT switching is from AP to P states. The RA product of the Gr barrier is set to be 1.5 $\Omega \cdot \mu m^2$. The pulse duration time is 5 ns.

AP state switching. In both cases, the $L1_0$-FePd/Gr, which has a high PMA, shows a slightly longer switching time than that of the $L1_0$-FePd. Figure 10(d) shows the STT-switching curves of the recording layer for a junction diameter of 7 nm. The STT-switching of 7 nm is as sharp as that of the 10 nm case. The STT-switching does not occur at the lowest voltage (1.0 V) in the case of 7 nm. The STT-switching started just before 5 ns at an applied voltage of 1.2 V. The magnetization

 © 2023 The Japan Society of Applied Physics

does not switch and returns to the original AP state when the applied voltage became zero at 5 ns. It is suggested that STT-switching is not completed until the z-component of magnetization is switched by around half. Figure 10(e) shows the relationship between the STT-switching time and the applied voltage estimated from the switching curves for both the AP and P states for the junction diameter of 7 nm. The $L1_0$-FePd/Gr with 7 nm tends to have a longer STT-switching time compared with 10 nm, especially at the low voltage region. Although this is thought to be due to an increase in Δ, there is a clear difference between the $L1_0$-FePd/Gr with a junction diameter of 7 nm and the 10 nm case.

Lowering the STT-switching voltage of the MTJs is required to reduce the load on the transistors. Several methods are proposed to increase the STT-switching efficiency and reduce switching voltage/current. One strategy is the double reference layer, which can theoretically increase the STT by a factor of 10.[82] It has been shown in experiments that the current density could be reduced by half.[83] This means that the STT-switching voltage can be reduced because the current density and voltage are in a proportional relationship. Another method to increase the STT-switching efficiency is to excite the initial magnetization movement by the processional spin current (PSC) layer. The magnetization of the PSC layer oscillates and assists the initial motion during the magnetization switching of the recording layer.[84] The PSC layer is magnetically coupled with the recording layer through the non-magnetic layer, and its main role is to reduce the incubation time by inducing magnetic precession of the recording layer by the PSC layer at the initial stage of STT-switching. The precession of magnetization begins slowly in the $L1_0$-FePd/Gr with high PMA, resulting in a long incubation time. The voltage is applied during the incubation time; shortening the incubation time can reduce electrical power consumption. Reducing incubation time contributes not only to reducing electricity consumption but also to a fast-switching speed. From the viewpoint of low power consumption, the precession energy of the PSC should be much smaller than the switching current of the recording layer. Thus, the PSC layer requires a low magnetic anisotropy, a low saturation magnetization, and a low α_{eff}. The PSC layer is excited faster than the recording layer, but the PSC layer can be excited separately with a pulse voltage lower than that of the recording layer. A single or double pulse for exciting the PSC layer is decided by the design of the circuit. In the actual stacking structure of an MTJ with the PSC layer, there are restrictions on material selection for the PSC layer due to the epitaxial growth of the $L1_0$-ordered alloy. The $L1_0$-ordered alloys can be grown epitaxially on Si/SiO_2 substrates when the proper cubic-based buffer materials are selected. The cubic-based ferromagnetic layer can be inserted as a PSC layer between the $L1_0$-ordered alloy and the Si substrate. The tetragonal/cubic ferromagnetic metals or tetragonal/cubic-based perovskite structures such as LSMO are candidates for the PSC layer. LSMO is expected to crystallographically grow epitaxially on a TiN buffer layer.[85] If the MRAM of MTJs is not used at high temperatures, as occurs in automatic driving, LSMO is an appealing material. The α_{eff} of the LSMO is on the order of 10^{-4},[86] which is comparable to low-damping ferromagnetic metals. In addition, Bi-substituted LSMO, in which Bi is replaced on the La sites, has a large magnetic refrigeration coefficient and can contribute to the cooling of the MTJs during the switching process.[87] Figure 11(a) shows the time dependence of the magnetization directions of the x-, y-, and z-components of MTJs. Each direction is the summation of all the magnetic layers of the MTJs. Thus, the magnetization oscillation of the x- and y-components is that of the PSC, and the z-component is mainly that of the $L1_0$-FePd recording layer. The 5 ns voltage is applied from 5 ns. The magnetic oscillation of the PSC layer of the x- and the y-components has periodicity before the magnetization switching of the recording layer. During STT-switching of the $L1_0$-FePd recording layer, the magnetization of the PSC layer is greatly disturbed. These facts indicated that the PSC layer and the $L1_0$-FePd recording layer are magnetically interactive through interlayer coupling. In this simulation, the PSC layer oscillated continuously for convenience, but in the real device, the oscillation is excited just before the voltage pulse is applied. To better understand the effect of the PSC layer, the STT-switching curves of the MTJs with and without the PSC layer are presented in the same figure. Figure 11(b) shows STT-switching curves of MTJs with a 10 nm junction diameter for the $L1_0$-FePd and $L1_0$-FePd/Gr with and without the PSC layer. The junction diameter is 10 nm, and the applied voltage is 1.0 V. Only the magnetization of the z-component is shown. It should be noted that the incubation time clearly decreased with the PSC layer in both the $L1_0$-FePd and $L1_0$-FePd/Gr recording layers. There are two switching phases in which the STT-switching gradually completes after the steep STT-switching in the case of MTJ with the PSC layer. This is because the magnetization oscillation of the PSC layer is strong. It can be considered that the gradual switching of the latter phase may be decreased by optimizing the oscillation intensity of the PSC layer. Figure 11(c) shows the STT-switching curves of the MTJs with a 7 nm junction diameter for the $L1_0$-FePd and $L1_0$-FePd/Gr recording layers with and without the PSC layer. The influence of the PSC effect was confirmed at 1.5 V because the $L1_0$-FePd/Gr was not switched at 1.0 V. The amount of STT-switching in the gradual change in the latter phase quantitatively decreased for the 7 nm diameter. This is because the energy required for switching at 7 nm is higher than that for 10 nm. The switching times of the $L1_0$-FePd and $L1_0$-FePd/Gr recording layers with 10 nm [Fig. 11(d)] and 7 nm [Fig. 11(e)] having the PSC layer are plotted. The trend of increasing the STT-switching time with decreasing voltage is the same as when there is no PSC layer, but the PSC layer decreases the switching time at any voltage. Therefore, the PSC layer is effective in reducing incubation time, power consumption, and applied voltage.

The SOT-MRAM has the advantage of having almost no incubation time due to the geometrical relationship of magnetizations. However, the SOT-MRAM is a three-terminal device, which requires a larger area than the STT-MRAM of a two-terminal device. It is difficult to replace STT-MRAM with SOT-MRAM from the viewpoint of high-density memory. The result of reducing the incubation time of the PSC layer in the STT-MRAM is important. As discussed in this study, many other technologies have been proposed for spintronics memory, and it is believed that the X-nm generation can be realized by using these technologies

 © 2023 The Japan Society of Applied Physics

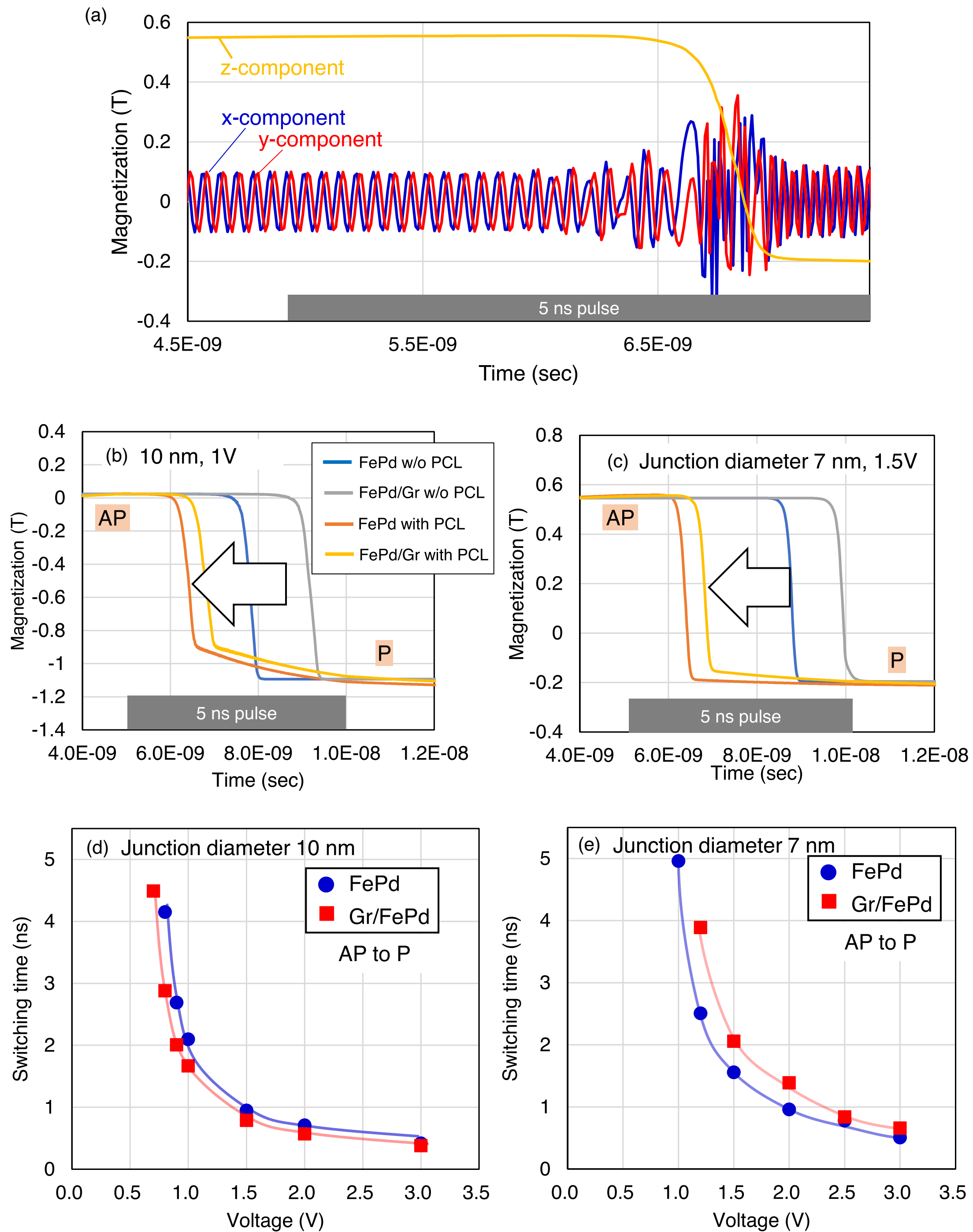

Fig. 11. (a) x, y, and z magnetization components during switching for the $L1_0$-FePd/Gr with PSC layer. The magnetization is the sum of both the PSC and $L1_0$-FePd layers. STT switching with (b) junction diameter of 10 nm and a film thickness of 2 nm and (c) junction diameter of 7 nm and a film thickness of 3 nm. For comparison, four types with and without the PSC layer and the Gr layer are shown. A voltage of 1 V was applied for 5 ns. The voltage dependence of switching time for (d) a junction diameter of 10 nm and a thickness of 2 nm with the PSC layer, and (e) the junction diameter of 7 nm and a thickness of 3 nm with the PSC layer. The STT switching is decided when the abrupt change occurred in the case of $L1_0$-FePd/Gr and $L1_0$-FePd with the PSC layer in (b).

in combinations, such as the simultaneous introduction of the PSC layer and the double reference layer. This study focused on the high PMA of bulk-ordered alloys with IPMA and predicted by simulation about the better data retention and switching efficiency in X-nm generation [red square in Fig. 2], but multi-layer IPMA systems and shape magnetic anisotropy are also strong candidates for the X-nm generation technologies. Especially in the first half of the X-nm generation, shape magnetic anisotropy is considered advantageous in terms of data retention characteristics. Given the remarkable growth of spintronic memory and the gradual increase in the commercialization market for spintronics memory, it is believed that hybrid technologies will take a definite stacking structure within the next few years.

4. Conclusions

MTJs with an $L1_0$-FePd recording layer and a Gr tunnel barrier are candidates for the X-nm generation of non-volatile magnetic spintronics memory. The hexagonal Gr is found to form on the tetragonal $L1_0$-FePd with an energetically stable interface, despite their completely different crystal symmetry, when the armchair axis of Gr is rotated 6.8° with the $(001)_{L10}$

© 2023 The Japan Society of Applied Physics

of $L1_0$-FePd. The IPMA exists at the interface between Gr and $L1_0$-FePd, which is owing to the shortening of the interlayer distance between Gr and $L1_0$-FePd, resulting in the formation of a chemisorption-type vdW force. Taking account of the IPMA in addition to the bulk $L1_0$-FePd PMA, micromagnetic simulation was used to calculate the data retention and the high-speed STT-switching characteristics. A realistic recording layer structure of MTJs with a junction diameter of 7 nm and a thickness of 3 nm, which is X-nm generation, can provide 10 year data retention. To deal with the increase in writing voltage due to the large magnetic anisotropy, a PSC layer is introduced into the micromagnetic simulation of magnetization switching. This PSC layer can reduce the load on the transistor. With the PSC layer, it is expected that high-speed switching of 2.2 ns at 1.5 V and 4 ns at 1.2 V will be achieved. $L1_0$-FePd/Gr has the potential to be used as a recording layer in the X-nm generation of non-volatile spintronics memory.

Acknowledgments

This study was partly supported by the Center for Spintronics Integrated Systems (CSIS) in Tohoku University, Japan Society for the Promotion of Science (JSPS) Core-to-Core Program (No. JPJSCCA20230005), QST-Tohoku University matching foundation, and the cross-appointment project in CSIS Tohoku University. This work has been performed under the approval of the Photon Factory Program Advisory Committee (No. 2019S2-003), nanotechnology platform at Tohoku University (No. A-20-TU-0063).

ORCID iDs

Hiroshi Naganuma https://orcid.org/0000-0003-2966-8269

1) C. A.-P. de Araujo, J. D. Cuchiaro, L. D. McMillan, M. C. Scott, and J. F. Scott, Nature **374**, 627 (1995).
2) M. Hosomi et al., IEEE Inter. Elec. Dev. Meeting (IEDM), Technical Digest, 2005, p. 473.
3) R. Waser and M. Aono, Nat. Mater. **6**, 833 (2007).
4) H.-S. Philip Wong, H.-Y. Lee, S. Yu, Y.-S. Chen, Y. Wu, P.-S. Chen, B. Lee, F. T. Chen, and M.-J. Tsai, Proc. IEEE **100**, 1951 (2012).
5) J.-G. Zhu and U. Zheng, J. Appl. Phys. **87**, 6668 (2000).
6) X. Dong, C. Xu, Y. Xie, and N. P. Jouppi, IEEE Trans. Cumput.-Aided Des. Integr. Circuits Syst. **31**, 994 (2012).
7) S. Bhatti, R. Sbiaa, A. Hirohata, H. Ohno, S. Fukami, and S. N. Piramanayagam, Mater. Today **20**, 530 (2017).
8) H. Honjo et al., IEEE Int. Electron Device Meeting (IEDM), Technical Digest, 2019, p. 28.5.1, 10.1109/IEDM19573.2019.8993443.
9) S. S. P. Parkin, C. Kaiser, A. Panchula, P. M. Rice, B. Jughes, M. Samant, and S.-H. Yang, Nat. Mater. **3**, 862 (2004).
10) S. Yuasa, T. Nagahama, A. Fukushima, Y. Suzuki, and K. Ando, Nat. Mater. **3**, 868 (2004).
11) J. C. Slonczewski, J. Magn. Magn. Mater. **159**, L1 (1996).
12) D. C. Ralph and M. D. Stiles, J. Magn. Magn. Mater. **320**, 1190 (2008).
13) M. Julliere, Phys. Lett. A **54**, 225 (1975).
14) S. Maekawa and U. Gafvert, IEEE Trans. Magn. **18**, 707 (1982).
15) M. N. Baibich, J. M. Broto, A. Fert, F. Nguyen Van Dau, F. Petroff, P. Etienne, G. Creuzet, A. Friederich, and J. Chazelas, Phys. Rev. Lett. **61**, 2472 (1998).
16) H. Naganuma, J. Inst. Elec. Info. Com. Eng. **101**, 1 (2023).
17) M. Natsui et al., Int. Solid-State Circuits Conf. (ISSCC), 2019, p. 202, 10.1109/ISSCC.2019.8662431.
18) V. B. Naik et al., 6th IEEE Electron Devices Technology Manufacturing Conf. (EDTM), 2022, p. 366, 10.1109/EDTM53872.2022.9798086.
19) T. Marinelli, J. G. Perez, C. Tenllado, M. Komalan, M. Gupta, and F. Catthoor, ACM Trans. Embed. Comput. Syst. **21**, 1 (2022).
20) D. Edelstein et al., Int. Electron Devices Meeting (IEDM), Technical Digest, 2020, p. 11.5.1, 10.1109/IEDM13553.2020.9371922.
21) S. Seo et al., Int. Electron Devices Meeting (IEDM), Technical Digest, 2022, p. 10.1.
22) S. M. Seo et al., IEEE Int. Electron Devices Meeting (IEDM), Technical Digest, 2022, p. 10.1.1, 10.1109/IEDM45625.2022.10019549.
23) S. Ikeda, K. Miura, H. Yamamoto, K. Mizunuma, H. D. Gan, M. Endo, S. Kanai, J. Hayakawa, F. Matsukura, and H. Ohno, Nat. Mater. **9**, 721 (2010).
24) H. Honjo et al., VLSI Symp. Technical Digest, 2015, p. 12.
25) S.-E. Lee, J.-U. Baek, and J. G. Park, Sci. Rep. **7**, 11907 (2017).
26) H. Sato, M. Yamanouchi, K. Miura, S. Ikeda, H. D. Gan, K. Mizunuma, R. Koizumi, F. Matsukura, and H. Ohno, Appl. Phys. Lett. **99**, 042501 (2011).
27) J. Swerts et al., IEEE Int. Electron Devices Meeting (IEDM), Technical Digest, 2017, p. 38.6.1, 10.1109/IEDM.2017.8268518.
28) H. Sato, M. Yamanouchi, S. Ikeda, S. Fukami, F. Matsukura, and H. Ohno, IEEE Trans. Magn. **49**, 4437 (2013).
29) K. Nishioka et al., IEEE Trans. Electron Devices **68**, 2680 (2021).
30) H. Naganuma et al., VLSI Symp. Technology Digest, 2021, p. T0179.
31) H. Honjo et al., Int. Electron Devices Meeting (IEDM), Technical Digest, 2022, p. 10.3.
32) K. Watanabe, B. Jinnai, S. Fukami, H. Sato, and H. Ohno, Nat. Commun. **9**, 663 (2018).
33) B. Jinnai, J. Igarashi, K. Watanabe, E. Christopher, I. Enobio, S. Fukami, and H. Ohno, Appl. Phys. Lett. **118**, 082404 (2021).
34) B. Jinnai, J. Igarashi, T. Shinoda, K. Watanabe, S. Fukami, and H. Ohno, Int. Electron Devices Meeting (IEDM), Technical Digest, 2021, p. 2.6.1.
35) R. Nandee, M. A. Chowdhury, A. Shahid, N. Hossainc, and M. Rana, Res. Eng. **15**, 100474 (2022).
36) F. Schwierz, Nat. Nanotechnol. **5**, 487 (2010).
37) S. Sahu and G. C. Rout, Int. Nano Lett. **7**, 81 (2017).
38) P. A. Khomyakov, G. Giovannetti, P. C. Rusu, G. Brocks, J. van den Brink, and P. J. Kelly, Phys. Rev. B **79**, 195425 (2009).
39) P.-C. Shen et al., Nature **593**, 211 (2021).
40) V. M. Karpan, G. Giovannetti, P. A. Khomyakov, M. Talanana, A. A. Starikov, M. Zwierzycki, J. van den Brink, G. Brocks, and P. J. Kelly, Phys. Rev. Lett. **99**, 176602 (2007).
41) T. M. G. Mohiuddin, E. Hill, D. Elias, A. Zhukov, K. Novoselov, and A. Geim, IEEE Trans. Magn. **44**, 2624 (2008).
42) E. Cobas, A. L. Friedman, O. M. J. Van't Erve, J. T. Robinson, and B. T. Jonker, Nano Lett. **12**, 3000 (2012).
43) J. Meng, J.-J. Chen, Y. Yan, D.-P. Yu, and Z.-M. Liao, Nanoscale **5**, 8894 (2013).
44) J.-H. Park and H.-J. Lee, Phys. Rev. B **89**, 165417 (2014).
45) B. Dlubak et al., ACS Nano **6**, 10930 (2012).
46) M.-B. Martin et al., Appl. Phys. Lett. **107**, 12408 (2015).
47) M. Piquemal-Banci et al., Nat. Commun. **11**, 5670 (2020).
48) V. Zatko et al., ACS Nano **16**, 14007 (2022).
49) H. Naganuma et al., Appl. Phys. Lett. **116**, 173101 (2020).
50) Y. Kota and A. Sakuma, J. Phys. Soc. Jpn. **83**, 034715 (2014).
51) K. Aledealat, B. Aladerah, A. Obeidat, and M. Gharaibeh, Heliyon **7**, e08639 (2021).
52) J. Robertso, H. Naganuma, and H. Lu, Jpn. J. Appl. Phys. **62**, SC0804 (2023).
53) H. Naganuma et al., Nano Lett. **15**, 623 (2015).
54) K. Amemiya, A. Toyoshima, T. Kikuchi, T. Kosuge, K. Nigorikawa, R. Sumii, and K. Ito, AIP Conf. Proc. **1234**, 295 (2010).
55) M. Sakamaki and K. Amemiya, Rev. Sci. Instrum. **88**, 083901 (2017).
56) See (http://fujitsu.com/global/about/resources/news/press-releases/2015/0324-01.html) for Fujitsu Ltd. (March 24, 2015).
57) H. Naganuma, H. Sato, S. Ikeda, and T. Endoh, AIP Adv. **10**, 075106 (2020).
58) H. Naganuma, H. Honjo, C. Kaneta, K. Nishioka, S. Ikeda, and T. Endoh, AIP Adv. **12**, 15317 (2022).
59) E. Weinan, W. Ren, and E. Vanden-Eijnden, J. Appl. Phys. **93**, 2275 (2003).
60) L. Maragliano, A. Fischer, E. V. -Eijnden, and G. Ciccotti, J. Chem. Phys. **125**, 024106 (2006).
61) H. Naganuma et al., ACS Nano **16**, 4139 (2022).
62) S. Ishio et al., J. Magn. Magn. Mater. **324**, 295 (2012).
63) J.-Y. Chiou, H. W. Chang, C.-C. Chi, C.-H. Hsiao, and C. Ouyang, ACS Appl. Nano Mater. **2**, 5663 (2019).
64) G. R. Trichya, J. Narayan, and H. Zhou, Appl. Phys. Lett. **89**, 132502 (2006).
65) G. R. Trichy, D. Chakraborti, J. Narayan, and J. T. Prater, Appl. Phys. Lett. **92**, 1022504 (2008).
66) H. H. Li, K. F. Dong, Y. G. Peng, G. Ju, G. M. Chow, and J. S. Chen, J. Appl. Phys. **110**, 043911 (2011).
67) E. Yang, S. Ratanaphan, J.-G. Zhu, and D. E. Laughlin, J. Appl. Phys. **109**, 07B770 (2011).

© 2023 The Japan Society of Applied Physics

68) H. Lu, J. Robertson, and H. Naganuma, Appl. Phys. Rev. **8**, 031307 (2021).
69) J. Ontaneda, F. Viñes, F. Illas, and R. Grau-Crespo, Phys. Chem. Chem. Phys. **21**, 10888 (2019).
70) M. Uemoto, H. Adachi, H. Naganuma, and T. Ono, J. Appl. Phys. **132**, 095301 (2022).
71) H. Yang, A. D. Vu, A. Hallal, N. Rougemaille, J. Coraux, G. Chen, A. K. Schmid, and M. Chshiev, Nano Lett. **16**, 145 (2016).
72) T. Watanabe et al., Appl. Phys. Lett. **112**, 022407 (2018).
73) M. Blanco-Rey et al., Appl. Nano Mater. **4**, 4398 (2021).
74) N. Rougemaille, A. T. N'Diaye, J. Coraux, C. Vo-Van, O. Fruchart, and A. K. Schmid, Appl. Phys. Lett. **101**, 142403 (2012).
75) Q. Cui, J. Liang, B. Yang, Z. Wang, P. Li, P. Cui, and H. Yang, Phys. Rev. B **101**, 214439 (2020).
76) M. Mulazzi et al., Phys. Rev. B **77**, 224425 (2008).
77) H. Shima, K. Oikawa, A. Fujita, K. Fukamichi, K. Ishida, and A. Sakuma, Phys. Rev. B **70**, 224408 (2004).
78) L. Thomas, G. Jan, S. Le, and P.-K. Wang, Appl. Phys. Lett. **106**, 162402 (2015).
79) K. Yakushiji, H. Kubota, A. Fukushima, and S. Yuasa, Appl. Phys. Express **9**, 013003 (2016).
80) H. Honjo, H. Naganuma, K. Nishioka, T. V. A. Nguyen, M. Yasuhira, S. Ikeda, and T. Endoh, IEEE Trans. Magn. **58**, 1400305 (2022).
81) W. Li, L. Xue, H. D. Abruna, and D. C. Ralph, Phys. Rev. B **89**, 184418 (2014).
82) D. C. Worledge, IEEE Magn. Lett. **8**, 4306505 (2017).
83) G. Hu et al., Int. Electron Devices Meeting (IEDM), Technical Digest, 2021, p. 2.5.1.
84) G. Wolf, B. Kardasz, J. Vasquez, T. Boone, D. Bozdag, S. Watts, J. Hernandez, P. Manandhar, Y.-T. Chin, and M. Pinarbasi, IEEE Magn. Lett. **11**, 4503404 (2020).
85) A. Tiwari, A. Chug, C. Jin, D. Kumar, and J. Narayan, Solid State Commun. **121**, 679 (2002).
86) Q. Qin, S. He, W. Song, P. Yang, Q. Wu, Y. P. Feng, and J. Chen, Appl. Phys. Lett. **110**, 112401 (2017).
87) K. Mizufune, H. Naganuma, S. Maruyama, and Y. Matsumoto, ACS Appl. Electron. Mater. **2**, 3658 (2020).

 © 2023 The Japan Society of Applied Physics